# Multi-length scale tomography for the determination and optimization of the effective microstructural properties in novel hierarchical solid oxide fuel cell anodes

Xuekun Lu [a], Oluwadamilola O. Taiwo [a], Antonio Bertei [b], Tao Li [c], Kang Li [c], Dan J.L. Brett [a], Paul R. Shearing [a, *]

[a] Electrochemical Innovation Lab, Department of Chemical Engineering, University College London, London, WC1E 7JE, UK
[b] Department of Earth Science and Engineering, Imperial College London, London, SW7 2AZ, UK
[c] Department of Chemical Engineering, Imperial College London, London, SW7 2AZ, UK

## HIGHLIGHTS

- SOFC anode with embedded micro-channels characterized by micro and nano tomography.
- Tortuosity factors decrease exponentially with the increase of electrode porosity.
- Embedded micro-channels enhance effective mass transport properties by 250%.
- Permeability improves by 2–3 orders of magnitude with the new electrode design.
- Multi-length scale tomography is essential for optimising hierarchical structures.

## GRAPHICAL ABSTRACT
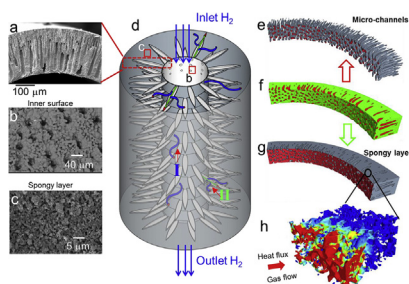


## ARTICLE INFO

## ABSTRACT

Effective microstructural properties are critical in determining the electrochemical performance of solid oxide fuel cells (SOFCs), particularly when operating at high current densities. A novel tubular SOFC anode with a hierarchical microstructure, composed of self-organized micro-channels and sponge-like regions, has been fabricated by a phase inversion technique to mitigate concentration losses. However, since pore sizes span over two orders of magnitude, the determination of the effective transport parameters using image-based techniques remains challenging. Pioneering steps are made in this study to characterize and optimize the microstructure by coupling multi-length scale 3D tomography and modeling. The results conclusively show that embedding finger-like micro-channels into the tubular anode can improve the mass transport by 250% and the permeability by 2–3 orders of magnitude. Our parametric study shows that increasing the porosity in the spongy layer beyond 10% enhances the effective transport parameters of the spongy layer at an exponential rate, but linearly for the full anode. For the first time, local and global mass transport properties are correlated to the microstructure, which is of wide interest for rationalizing the design optimization of SOFC electrodes and more generally for hierarchical materials in batteries and membranes.

© 2017 The Authors. Published by Elsevier B.V. This is an open access article under the CC BY license (http://creativecommons.org/licenses/by/4.0/).

## 1. Introduction

Solid Oxide Fuel Cells (SOFCs) are one of the most promising electrochemical devices for the efficient co-generation of heat and electricity operating on a range of fuel gases [1,2]. Concentration polarization is one of the three main loss mechanisms in SOFCs [3,4]. It arises from slow gas-phase mass transport processes, which results in a concentration gradient of reactants and products at the chemically active sites.

Gas transport in porous electrodes mainly depends on pressure, temperature, and gas species as well as the microstructural properties of the electrodes, such as porosity ($\varepsilon$), pore size ($d$) and hence the permeability ($k$) [5-7] and tortuosity factor ($\tau$) which is often used to characterize gas diffusion resistance due to the tortuous pore volume [6,8,9].

These effective transport parameters can be obtained by image analysis [10,11] and modeling of mass/heat flux on the 3D microstructure of the porous phase [6,12] acquired by X-ray computed tomography or FIB-SEM (focused ion beam scanning electron microscope). Additionally, permeability is an important effective transport parameter describing the resistance of the viscous flow in the porous electrodes [13]. Viscous flow can occur to balance the pressure gradient of gas species with different molecular weights, such as $H_2$ and $H_2O$ [14]. A simple one dimensional Dusty Gas Model (DGM) calculation for a $H_2(97\%)/H_2O(3\%)$ mixture shows that the pressure-driven backflow of $H_2O$ can be up to 10% of the total $H_2O$ molar flux in the working conditions reported by Bertei et al. [14]. Such a permeation flux term is often erroneously neglected in the literature, especially when applying the DGM, resulting in an inaccurate prediction of concentration losses with errors as large as 20–60% [15,16].

Tubular SOFCs offer a number of advantages over their monolithic and planar counterparts, including higher volumetric power densities, lower cost of manufacture, ease of gas sealing and higher thermal resilience [17]. Recently a novel, hollow fiber tubular anode-supported SOFC (HF-SOFC) fabricated by a phase inversion (PI) technique, has attracted increasing attention [17-19]. Compared to a conventional tubular SOFC anode, which consists of a symmetric sponge-like porous structure (pore diameter $d \approx 0.2\ \mu m$), the spongy anode of the HF-SOFC is embedded with radially aligned micro-channels ($d \approx 20\ \mu m$) for the purpose of enhanced mass transport. Fig. 1a,b and c are SEM images showing the local microstructures at the corresponding sites in Fig. 1d. Due to the distinct difference in pore sizes, the trajectories of the fuel gas are different in each region. For conventional tubular SOFCs, the fuel gas travels in the tortuous spongy layer (i.e. the electrochemically active region) according to trajectory I. On the contrary, the introduction of the micro-channels in the HF-SOFC greatly
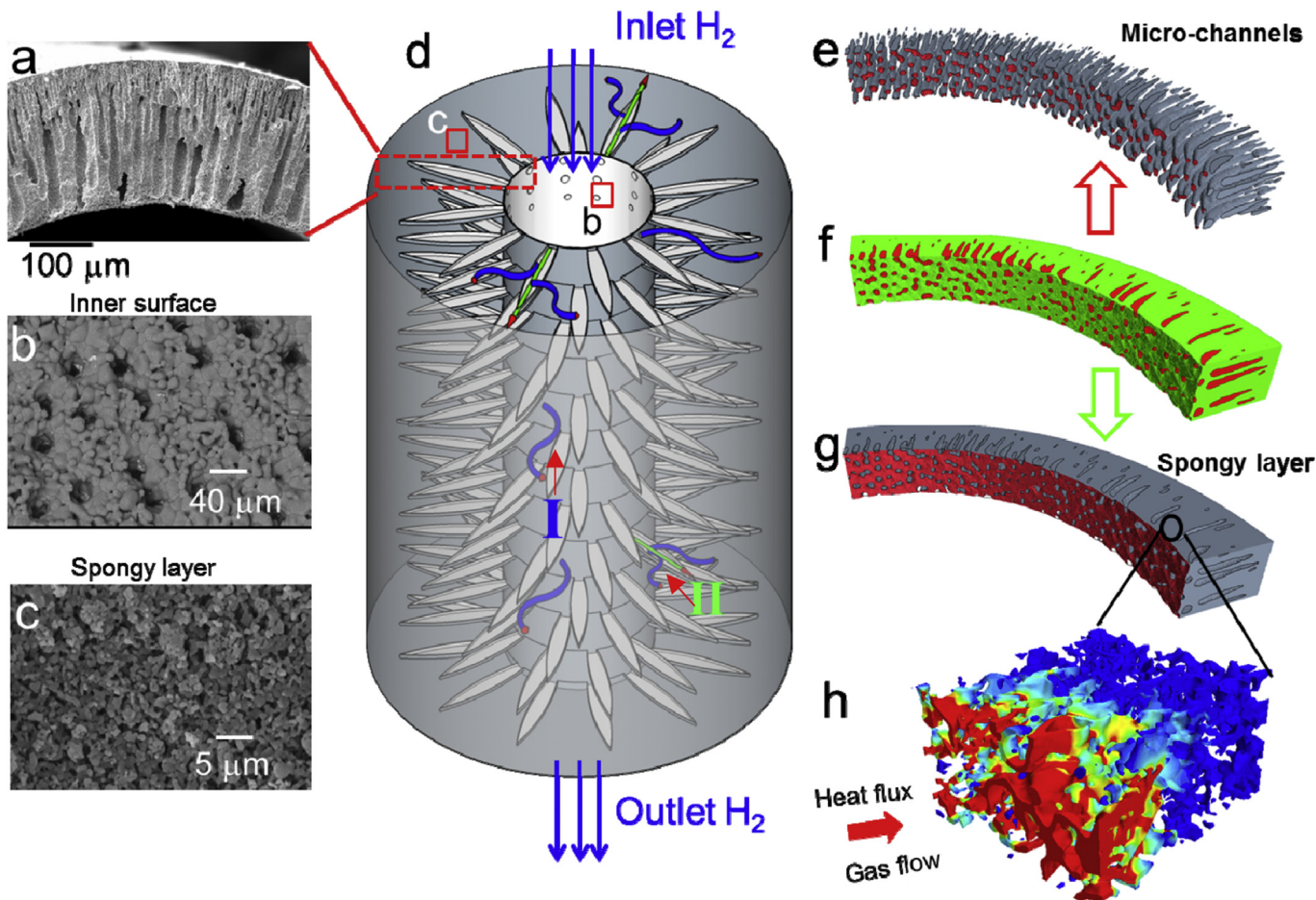


**Fig. 1.** (a)–(c) SEM images showing the hierarchical microstructures at the corresponding sites in (d) schematic illustration of HF-SOFC anode. The green and blue arrows indicate the gas flow trajectories at different regions of significantly different pore sizes; (f) Micro-CT data showing the full thickness of the anode, composed of the micro-channels (red) and spongy layer (green). Each region has independent effective transport properties, as is shown in (e) and (g). (h) Nano-CT scan showing the pore phase in the spongy layer, which is used for heat flux and gas flow simulation to extract the local effective transport parameters. (For interpretation of the references to colour in this figure legend, the reader is referred to the web version of this article.)

mitigates the resistance of the gas flow from the centre bore to the anode/electrolyte interface as the gas molecules preferentially flow through the micro-channels first and then access the interface by diffusion, shown as trajectory II (Fig. 1d).

It is important to obtain the effective transport parameters of the spongy layer (i.e. $\tau_s$, $k_s$ in the green region of Fig. 1f) in order to estimate the representative effective transport parameters for the full anode and thus assess the overall benefits of the hierarchical structure. However, the large difference of the pore diameter between the micro-channels (Fig. 1e) and spongy layer (Fig. 1g) makes it impossible to resolve them simultaneously due to the trade-off between image field of view (FOV) and resolution. This means the two flow domains have to be characterized independently in order to extract the microstructure parameters for the anode. Previous work by Cooper et al. [20] estimated the tortuosity factor of the full anode by empirically assigning an effective diffusivity of the spongy layer; however, in this study, we develop this methodology further to account for the inherent hierarchical microstructure using a multi-length scale approach.

Here, we have conducted for the first time a multi-length scale, non-destructive X-ray computed tomography (X-ray CT) imaging approach for the full anode (using micro-CT, Fig. 1f) and spongy layer (using nano-CT, Fig. 1h) respectively. This enables a unique, coupled approach to modeling the global effective transport properties of the fuel cell, whilst simultaneously accounting for local microstructural complexity. Firstly, using the nano-CT data, the heat flux analogy and gas flow simulations are performed using the 3D microstructure of the spongy layer (Fig. 1h), which are then used to define the effective transport parameters (i.e. tortuosity factor, permeability and porosity) of the spongy layer (Fig. 1g). The full-anode simulation (using both the heat flux analogy and gas flow simulations) is conducted using the micro-CT data of the full HF-SOFC (Fig. 1f) with the spongy layer represented by an effective medium correction to the solid phase (the green region in Fig. 1f), using effective transport parameters as an input obtained from the nano-CT simulations. By using this mean-field average approach in multi-length scale tomography, the representative effective transport parameters describing the overall capability of the fluid flow in the full anode can be obtained: this is crucial for the electrochemical performance simulation and evaluation of concentration polarization losses in the HF-SOFC. Furthermore, a parametric study is also conducted to reveal the variation of the effective transport parameters related to the porosity and pore size of the spongy layer, which will provide insights for optimization of microstructure control in the fabrication process. It is worth mentioning that this study focuses on species-independent effective transport parameters (i.e. $\tau$ and $k$), which are the baseline of the microstructure properties. Any species-dependent contributions, such as Knudsen effects, can be evaluated separately.

## 2. Experimental

### 2.1. Materials

Commercially available powders of yttria-stabilized zirconia (8YSZ, mean particle size 0.1—0.4 $\mu$m) and nickel oxide (NiO, mean particle size 0.5—1.5 $\mu$m) were purchased from Inframat Advanced

Materials and used as supplied. Polyethersulfone (PESf) (Radal A300, Ameco Performance, USA), 30-dipolyhydroxystearate (Arlacel P135, Uniqema), and N-methyl-2-pyrrolidone (NMP, HPLC grade, VWR) were used as the polymer binder, dispersant, and solvent, respectively. A suspension composed of ceramic particles (60% wt. NiO), solvent and polymer binder was mixed for 3—4 days via planetary ball milling (SFM-1 Desk-top Miller, MTI Corporation, USA) to assure homogeneity, and was subsequently degassed under vacuum to fully eliminate air bubbles trapped inside. This suspension was then applied with an internal coagulant (polyvinyl alcohol (PVA, M.W. approx. 145000, Merck Schuchardt OHG, Germany) in a phase inversion technique [21-25]. The fabricated HF-SOFC is embedded with radial 'finger-like' micro-channels as a consequence of the solvent/non-solvent exchange. The tube was sintered at 1200 °C for 6 h, followed by the reduction at 700 °C for 2.5 h.

### 2.2. X-ray computed tomography (X-ray CT)

The entire tubular anode was imaged in 3D using a Versa 520 X-ray microscope (micro-CT) and a randomly-selected portion of the spongy layer, big enough to be statistically representative as shown in a previous report [26] was imaged using an Ultra 810 X-ray microscope (nano-CT; both Zeiss Xradia, Carl Zeiss, CA, USA) [27]. Detailed scanning parameters are shown in Table 1. Proprietary Feldkamp-Davis-Kress (FDK) and filtered-back projection algorithms were used for the reconstruction of the full anode and the spongy layer scans respectively [28,29]. The reconstructed sample volumes were segmented into solid and pore phase using watershed method in the Avizo V9.0 software (FEI, Bordeaux) package. The binary image stacks of the spongy layer were imported into Fiji [30] for the pore diameter and porosity measurement.

### 2.3. Heat transfer and gas flow simulation

#### 2.3.1. Tortuosity factor and permeability

The analogy between heat and mass transfer is well established [6,31] and is regularly used to measure the tortuosity factor. The heat flow driven by a temperature gradient in a fully porous volume is described by Fourier's law as

$$Q_b = -A\sigma\frac{\Delta T}{L} \tag{1}$$

where $A$ is the cross-sectional area of the flow volume, $\sigma$ is the thermal conductivity of the porous phase, $\Delta T$ is the temperature difference and $L$ is the length of flow volume. If the heat flow takes place in a porous medium, Eq. (1) is modified as

$$Q_p = -A\frac{\varepsilon}{\tau}\sigma\frac{\Delta T}{L} \tag{2}$$

where $\varepsilon$ is the porosity and can be measured by image analysis. $\tau$ is the tortuosity factor. By dividing $Q_p$ by $Q_b$, the effective transport parameter $\varepsilon/\tau$ can be obtained by Equation (3),

$$\frac{Q_p}{Q_b} = \frac{\varepsilon}{\tau} \tag{3}$$

**Table 1**
Scanning parameters for the spongy layer and full anode.

|  | Voxel size ($\mu$m) | Field of view ($\mu$m$^2$) | Projections | Exposure time (s) | Camera binning |
|---|---|---|---|---|---|
| Spongy Layer | 0.032 | 16 × 16 | 1201 | 60 | 2 |
| Full Anode | 1.07 | 2140 × 2140 | 2001 | 18 | 1 |

For mass transport in porous electrodes, the Reynold's number [32] is far less than unity, which suggests that viscous forces dominate over inertial forces and a fluid is said to be in the creeping flow regime. The permeability can be obtained according to Darcy's law [33],

$$\frac{\partial P}{\partial x} = -\frac{\mu}{k} v \qquad (4)$$

where $\mu$ is the dynamic viscosity of the fluid, $v$ is the volume-averaged velocity, $k$ is the permeability of the porous medium, $P$ is the pressure and $x$ is the distance in the flow direction. In this study, $k$ is measured by assigning pressure drop ranges from 20 to 10 kPa as the boundary conditions, thus covering the pressure gradient range in a $H_2/H_2O/N_2$ gas mixture in typical operating conditions [14]. The plot of pressure drop vs. velocity is fitted to obtain $k$, which is independent of the pressure drop in laminar regime.

### 2.3.2. Image-based simulation

The reconstructed 3D volume of the anode (micro-CT) and spongy layer (nano-CT) are imported to the CFD software Star-CCM+ (CD-adapco Inc., London) for the simulation. This concept, which effectively combines image data across multiple length scales (from micro and nano-CT), is illustrated in Fig. 1e–h: the anode with an axial depth of 700 μm and 90° arc angle is modelled as the flow domain (Fig. 1f). It is composed of two parts: the micro-channels (red) and the porous spongy layer (green). The two sub-domains are defined independently: the micro-channels are regarded as open porous phase (conductivity σ, infinite permeability, Fig. 1e) while the effective transport parameters in the porous spongy layer (Fig. 1g) are obtained using the heat transfer analogy simulation (Eq. (3)) and gas flow simulation using Darcy's law (Eq. (4)) modelled using the microstructural framework provided by the nano-CT scan (Fig. 1h).

Thus the conductivity and permeability in the spongy layer of the full thickness simulation are defined as $\varepsilon_s/\tau_s \cdot \sigma$ and $k_s$ respectively. For simplicity, the conductivity of the open porous phase is set to unity (i.e. $\sigma = 1$). The detailed simulation parameters are shown in Table 2. Video 1 illustrates the technique of multi-scale coupling simulation as well as the workflow in this study.

Supplementary video related to this article can be found at https://doi.org/10.1016/j.jpowsour.2017.09.017

A parametric study is also conducted to correlate the variation of porosity in the spongy layer to the effective transport parameters and to explore its effect on the global transport properties of the HF-SOFC. Morphological operations (e.g. erosion and dilation) [34] are performed on the segmented binary data of the spongy layer to

**Table 2**
Parameters and conditions of the heat flux and gas flow simulations for the spongy layer and entire anode.

| | Spongy layer | Full anode |
|---|---|---|
| Mesh type | Polyhedral volume mesh | Polyhedral volume mesh |
| Number of cells | 1.2 million | 1.6 million |
| Inlet temperature (K) | 1000 | 1000 |
| Outlet temperature (K) | 300 | 300 |
| Thermal conductivity | $\varepsilon_s/\tau_s$ | Microchannels: 1 Spongy layer: $\varepsilon_s/\tau_s$ |
| Pressure drop (Pa) | 20 to 10 k | 20 to 10 k |
| Permeability | $k_s$ | Micro-channels: fully porous Spongy layer: $k_s$ |
| Sample dimension ($\mu m^3$) | 9 × 6 × 4 | 843 × 843 × 700 |

achieve porosity ranges from 5% to 48% while keeping the morphology of the solid phase constant.

## 3. Results and discussion

### 3.1. Multi-length scale X-ray CT

The hierarchical microstructure of the HF-SOFC anode is shown in Fig. 2. Fig. 2a shows the 3D rendering of the full anode from micro-CT data where the porous entrances of the micro-channels at the inner wall of the tube can be observed. The radially grown micro-channels which originate from the centre bore are clearly resolved, but the spongy layer appears to be solid, as its pores are too small to be seen at this resolution (Fig. 2b). Small pores are captured at a higher resolution with nano-CT imaging on a small piece of the sample extracted from the spongy layer (Fig. 2c). The contrast is good enough so that the Ni (dark grey), the YSZ (light grey) and the porous phase can be distinguished [35]. The porosity of the spongy layer is measured from the segmented nano-CT data to be 19 %.

In order to study the effect of porosity ($\varepsilon$) and pore sizes ($d$) on the effective transport properties, the porous phase of the original sample was used as 'seed' data for morphological erosion/dilation. These morphological operations, which isotropically shrink/grow the pore size to mimic densification during sintering, provide a range of porous microstructures of different porosities for the purposes of a parametric investigation (Fig. 2d–f). The information of different samples is listed in Table 3. It should be pointed out that no percolation is found in the sample with 5% porosity and this is consistent with the results in the literature [36,37].

### 3.2. Computed fluid dynamics simulation

#### 3.2.1. Spongy layer (nano-CT): tortuosity factor vs. porosity

The heat transfer simulation was first conducted on the porous phase of the spongy layer. It is worth recalling here that the simulation was performed without taking into account Knudsen diffusion in order to obtain species-independent results. In a previous report' [26] the authors evaluated the Knudsen number distribution in the spongy layer, being within 1.1–4.8 (i.e., in transition regime) for hydrogen within 600–1000 °C at 1 atm. Notably, the tortuosity factor is independent of the Knudsen number for porosities above 15% when the characteristic length-scale of the pore phase is properly chosen, as shown by Zalc et al. [37].

Fig. 3a shows the distribution of temperature and the heat flux based on the operating boundary conditions. It is observed from Fig. 3b, that the tortuosity and constrictivity [38] of the pore network lead to a heterogeneous distribution of the flux, and the local flux maxima appear at the pore throats.

The dependence of tortuosity factor $\tau_s$ and effective transport parameter $\varepsilon_s/\tau_s$ with porosity $\varepsilon_s$ are plotted in Fig. 4. A steep increase in $\tau_s$ and corresponding drop in $\varepsilon_s/\tau_s$ are observed as the porosity is reduced from 19% to 10% which could be the result of low connectivity of the 10% porosity sample (see Table 3). This is in agreement with the literature showing that the pore percolation threshold is 5–10% and the percolation ratio is above 99% at 25% porosity [39,40]. The tortuosity factor of the original dataset with 19% porosity ($\tau_s = 12.3$) is consistent with those reported in the literature [41-43], and the $\varepsilon_s/\tau_s$ is measured to be 0.015. The effective transport parameter $\varepsilon_s/\tau_s$ of the spongy layer can be interpolated with Archie's law [44], which gives the exponent of 2.33. This is slightly larger than that in Bruggeman's prediction [45-47], although not dissimilar from what obtained by Berson et al. [45] in synthetic microstructures.
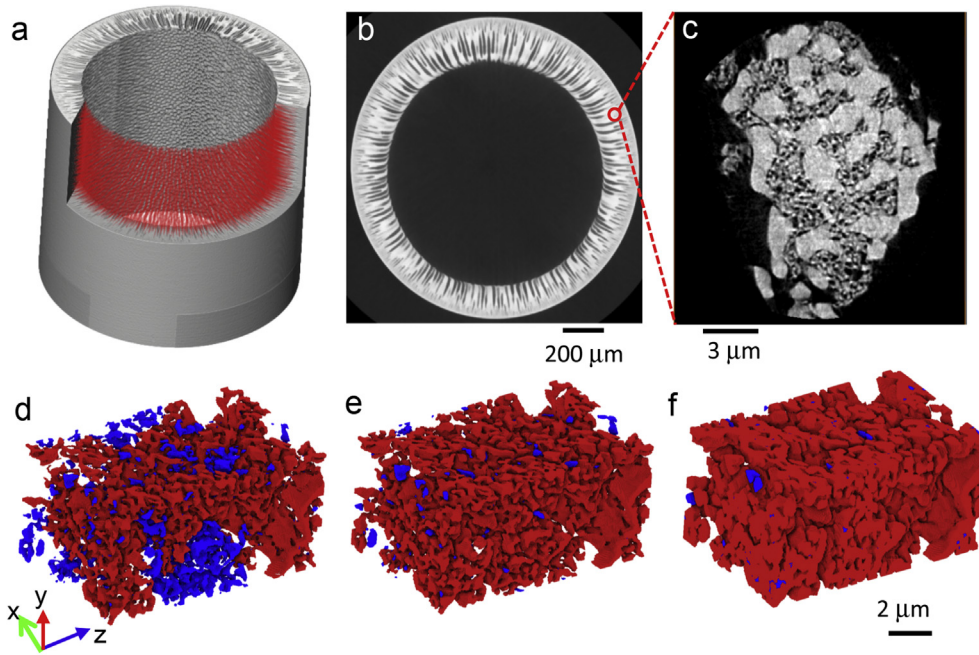
**Fig. 2.** The hierarchical microstructure of the HF-SOFC anode: (a) 3D volume rendering of the entire anode with micro-channels highlighted in red in the control volume, (b) a virtual slice of the full anode scanned at the resolution of 1.07 μm, and (c) spongy layer in the anode scanned at the resolution of 0.032 μm (the brighter phase is YSZ while the darker porous phase is Ni). Segmented porous phase with the porosity of (d) 10% (e) 19% (original data) (f) 48% are obtained by morphological operations for the parametric investigation. Red and blue phases represent the percolated and non-percolated pores respectively. (For interpretation of the references to colour in this figure legend, the reader is referred to the web version of this article.)

**Table 3**
Parameters of the porous phase in the spongy layer of different porosities: $d$ represents the mean pore diameter, $c$ the connectivity (i.e., the fraction of percolating pores).

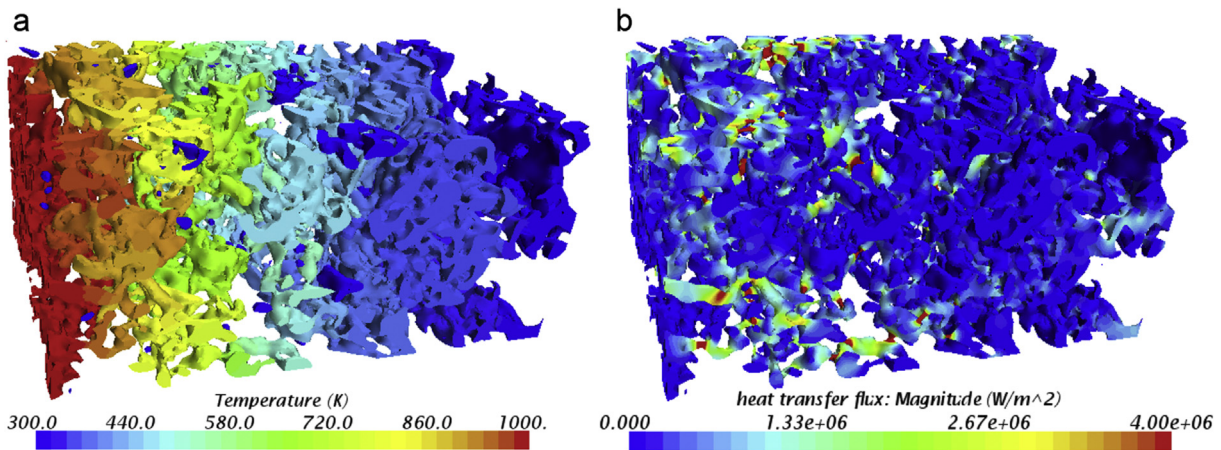| $\varepsilon$ | 5 % | 10 % | 19 % | 28 % | 39 % | 48 % |
|---|---|---|---|---|---|---|
| $d$ (μm) | 0.1± 0.03 | 0.15 ± 0.05 | 0.18 ± 0.05 | 0.23 ± 0.05 | 0.27 ± 0.07 | 0.33 ± 0.08 |
| $c$ | 0 % | 91.1 % | 99.1 % | 99.5 % | 99.7 % | 99.9 % |



**Fig. 3.** (a) Temperature and (b) heat flux distribution in the porous phase of the spongy layer with 19% porosity. Note that the temperature field here is equivalent to the distribution of any scalar variable (e.g. concentration) modelled using continuum diffusion.

### 3.2.2. Spongy layer (nano-CT): permeability vs. porosity

Permeability characterizes the viscous resistance to the fluid flow in the porous medium. Viscous flow is often neglected when the mass transport is solved by Fick's law without consideration of Knudsen effects. However, viscous flow can play a significant role for non-equi-mass counter diffusion [48], which is the case for SOFC electrodes. In addition, for these HF-SOFCs, pressure-driven convection can be the dominant gas transport mechanism within the wide micro-channels at the inner wall of the tubular anode. A range of different pressure gradients were applied as boundary conditions in the fluid domain for the samples of different porosities. Fig. 5 demonstrates that the overall flow velocity increases with the porosity as it provides better percolation and more junctions among the pathways. For example, the region indicated by a
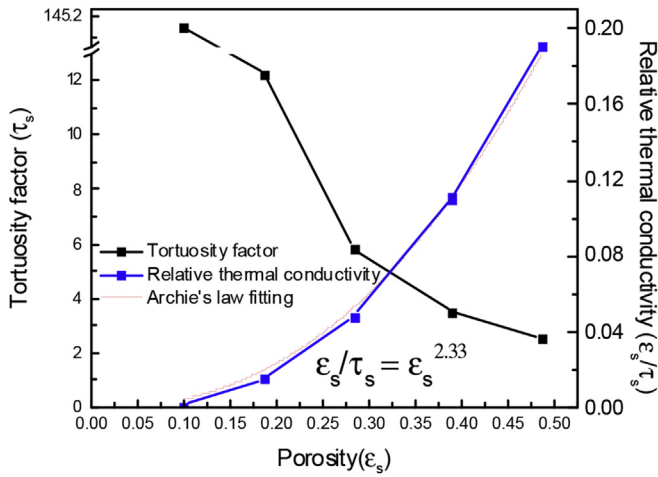
**Fig. 4.** Tortuosity factor ($\tau_s$) and relative thermal conductivity ($\varepsilon_s/\tau_s$) of the spongy layer are plotted against porosity $\varepsilon_s$. $\varepsilon_s/\tau_s$ can be well predicted using Archie's law with the exponent of 2.33.



**Fig. 6.** Pressure drop *vs.* velocity for spongy layer samples of different porosities.

black arrow in Fig. 5a displays little flow, due to the poor percolation and dead-end pores, but this is greatly improved in high porosity samples.

The relationship between the pressure drop and velocity for the samples of different porosity are plotted in Fig. 6. The permeabilities, fitted with Darcy's law (Eq. (4)), for different samples are listed in Table 4 and compared with the predictions using the Carman-Kozeny model [49,50]. It is seen that the measured permeabilities are consistent with the predicted values for high porosity samples (i.e. $\varepsilon_s$ = 39% and 48%). Discrepancies are found for the lower porosity samples, which may arise from the ambiguity of the shape factor used in the Carman-Kozeny model. The shape factor is a dimensionless parameter that represents the geometrical information of the flow channel and it varies with the medium
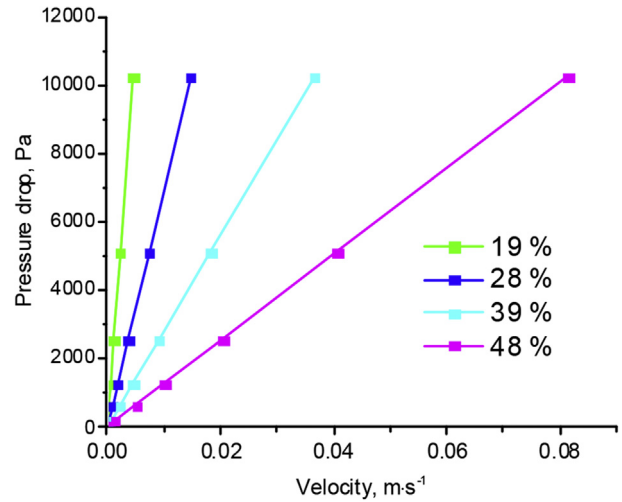
homogeneity, constriction effects and packing arrangement of the solid phase [49,51]. This value is reported empirically to be between 40 and 160 for the different porous microstructures and an approximated value of 52 is used here according to Yazdachi's theory [49]. The measured results are in good agreement with the values for Ni-YSZ anode reported in the literature [52].

### 3.2.3. Full anode (micro-CT): temperature and pressure distributions

Fig. 7a–c shows the temperature distributions of three cases with different porosities of the spongy layer. It should be mentioned that the temperature distribution here is equivalent to the distribution of any scalar variable (e.g. concentration) modelled using continuum diffusion. Similarly, the applied temperature
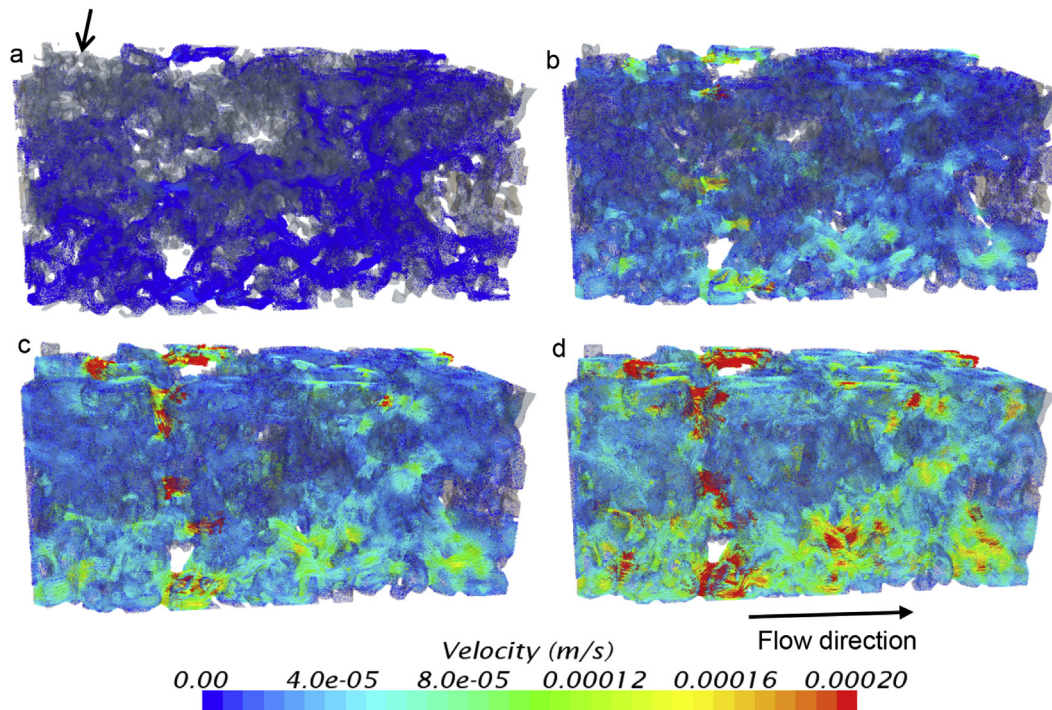


**Fig. 5.** H$_2$ flow through the porous spongy layer anode at the pressure drop of 50 Pa for the sample porosities of (a) 19% (b) 28% (c) 39% and (d) 48 %.

**Table 4**
Permeabilities for spongy layer samples of different porosities.

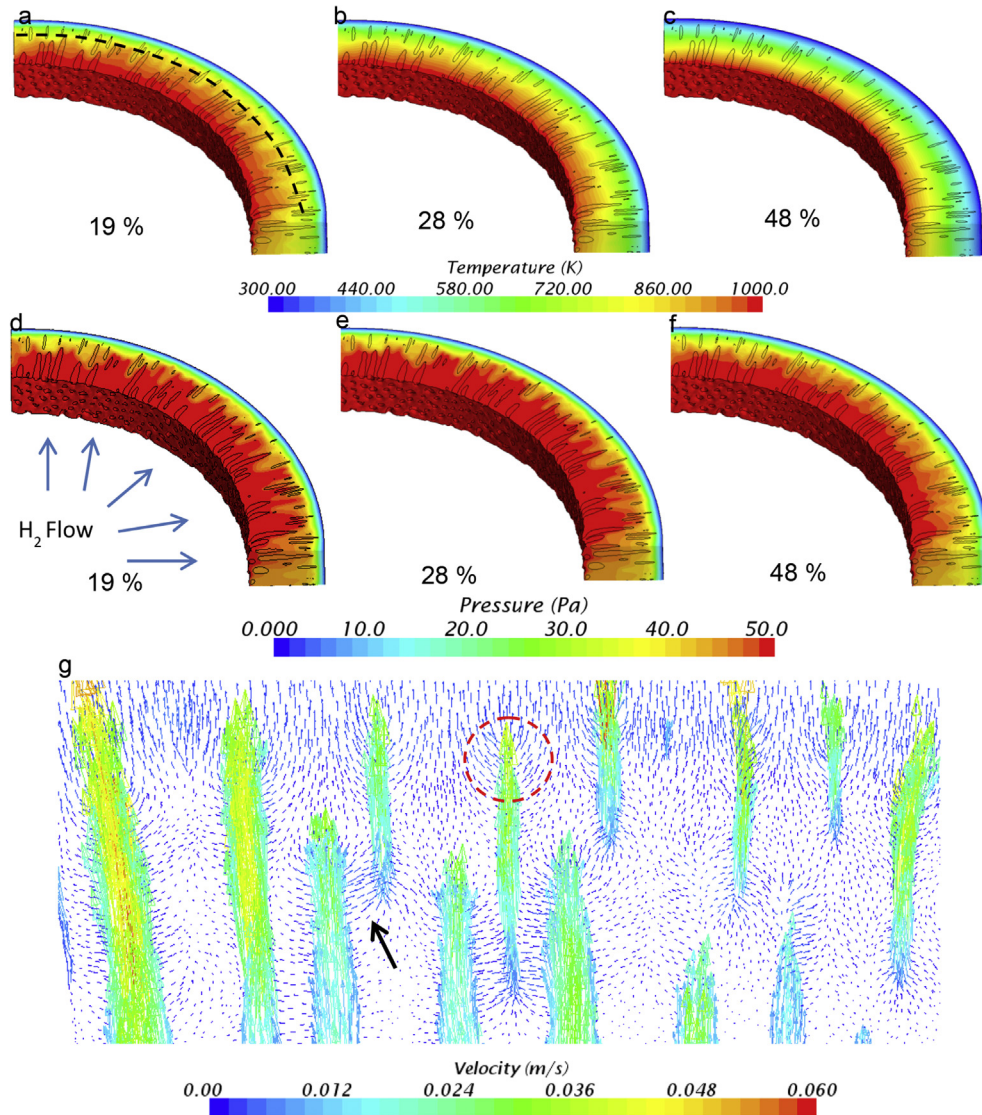| Porosity | 19 % | 28 % | 39 % | 48 % |
|---|---|---|---|---|
| Permeability ($m^2$) | $3.1 \times 10^{-17}$ | $1.0 \times 10^{-16}$ | $2.5 \times 10^{-16}$ | $5.6 \times 10^{-16}$ |
| Carman-Kozeny model ($m^2$) | $7.05 \times 10^{-18}$ | $4.21 \times 10^{-17}$ | $2.01 \times 10^{-16}$ | $5.73 \times 10^{-16}$ |



**Fig. 7.** Temperature distribution of the full anode heat transfer simulation (a–c) and the pressure distribution of the gas flow simulation (d–f) for different porosities of the spongy layer. The dashed curled line in (a) indicates the boundary of the inner region rich in active micro-channels and outer region which consists of isolated micro-channels and the spongy layer. (g) shows the vector field of the gas velocity. Gas molecules migrating from active micro-channels to the spongy layer are marked by the red circle and those migrating to the isolated micro-channels are pointed by the black arrow. (For interpretation of the references to colour in this figure legend, the reader is referred to the web version of this article.)

range (300–1000 K here) does not make any difference in the distribution as it will affect only the upper and lower bounds of the colormap. There are three main observations from these results: 1) the global temperature is higher when the porosity of the spongy layer is lower; 2) the temperature gradient in the radial direction is more uniform when the porosity of the spongy layer is higher, while the temperature is inhomogeneous (i.e. flat in the inner region and steep in the outer region) when the porosity is lower; 3) there is an evident variation in temperature distribution in the hoop direction when the porosity is lower (see Fig. 7a).

The temperature field can be explained by dividing the anode into two sub-regions aligned in series along the radial direction (indicated by the black dashed line in Fig. 7a): the inner region, embedded with active micro-channels originating from the inner wall, and the outer region, with few active micro-channels. Continuum fluid physics suggests that the heat flow in the inner region and the outer region must be equal and are represented by Fourier's law (Eq. (1)) as $\sigma_i A_i \Delta T_i / L_i = \sigma_o A_o \Delta T_o / L_o$ ($i$ for inner, $o$ for outer). As the inner region has a higher effective thermal conductivity than the outer region ($\sigma_i > \sigma_o$) due to the percolating micro-channels, while

the cross sectional area $A_i \approx A_o$, the temperature gradient of the outer region is steeper. The temperature drops from 700 K to 300 K within only one-third of the anode thickness. This phenomenon is more apparent in the sample of 19% porosity, which shows the largest difference in the effective thermal conductivity between the two regions and accordingly demonstrates a flat temperature gradient at the inner region and higher gradient at outer region. This disparity is mitigated as the porosity of the spongy layer increases, due to a larger effective thermal conductivity of the outer layer and a smaller conductivity difference between the two regions. This is why the sample with 48% porosity displays the most homogeneous temperature gradient distribution.

In the hoop direction, the spongy layer and the micro-channels are aligned in parallel alongside each other. Owing to a significant conductivity difference, most of the heat tends to flow through the micro-channels, where the temperature is almost uniform, and the temperature of the adjacent spongy layer appears to be the same as the contacting micro-channels. Therefore, the micro-channels and the spongy layer behave according to an electrical circuit analogy with two parallel resistances: both the domains share the same temperature but only the most-conducting one (i.e., the micro-channels) carries the majority of the heat flux. However, where a micro-channel terminates, the accumulated heat flux in the active micro-channel is transferred to the neighboring isolated micro-channels in the hoop direction by flowing through the high-resistance spongy layer, thus causing the sharp temperature gradient in the hoop direction observed for low porosity of the spongy layer (Fig. 7a).

Good agreement is found in the gas flow simulation (see Fig. 7d–f), which was conducted by assigning the permeabilities and porosities of the spongy layers to the solid phase and the micro-channels are treated as fully porous space. The result shows that the inner regions display a more uniform distribution of pressure with lower gradient compared to the temperature in the heat transfer simulation. The pressure merely drops 20% before reaching the outer region. Fig. 7g displays the vector field of the gas flow on the cross section of the anode. It is noted that the velocity of the molecules is significantly larger in the micro-channels than in the spongy layer. When aligned in parallel with the spongy layer of high viscous resistance, the micro-channels carry most of the gas molecules. Besides, gas molecules tend to migrate to the spongy region from micro-channels sideways (marked by a red dashed circle) as well as migrate into the isolated micro-channels (black arrow).

### 3.2.4. Full anode (micro-CT): tortuosity factor and permeability vs. porosity

The tortuosity factor obtained from the spongy layer and the characteristic tortuosity factor from the full anode are plotted against the porosity of the spongy layer in Fig. 8a. It is seen that the representative tortuosity factors of the full anode are lower than that of the spongy layer for all porosity samples. Initially, the tortuosity factors are remarkably large at 10% porosity, followed by a sharp drop to a value ten times smaller at 19% porosity. Generally, the tortuosity factors decrease with increasing porosity, but the large change from 10% to 19% is also supported by the enhancement in pore connectivity from 91% to 99% within the spongy layer. The relative thermal conductivity obtained by Eq. (3) is shown in Fig. 8b as a function of porosity. It is evident that the transport property of the tubular HF-SOFC anode is improved by approximately 200% compared with the traditional tubular SOFC consisting mainly of the spongy layer. The relative thermal conductivity of the full anode can be predicted by a linear relation with the porosity, compared to the exponential relation with the porosity of the spongy layer. A significant difference of the representative permeability of the

entire anode and of the spongy layer is found in Fig. 8c. The inclusion of the micro-channels effectively increases the permeability of the anode by 2–3 orders of magnitude, which will greatly improve the mass transport in the anode and thus reduce the onset of mass transport limiting current.

As mentioned previously, only microstructural-dependent transport properties are evaluated in this study to guide the electrode fabrication, although the species-dependent contributions can be added separately to consider different fuel gas mixtures. It is noted in Fig. 8b that the measured relative thermal conductivity of the entire anode falls between the Wiener bounds [53,54], which is consistent with the physical limits of the relative thermal conductivity. The difference between the Wiener upper bound and the relative thermal conductivity of the entire anode represents the possible further improvement achievable by changing the arrangement of micro-channels in the entire anode. As is evident from Fig. 7, there are some non-percolating isolated micro-channels, which cause the transfer of flow among micro-channels to be heavily dependent on the spongy layer placed in between. These isolated micro-channels prevent the relative thermal conductivity of the entire anode from approaching the Wiener upper bound. As the spongy layer porosity increases, the difference between the upper bound and the relative conductivity of the entire anode decreases, indicating that a change in the arrangement of the micro-channels would not be necessary in such as case since the high-porosity spongy layer is capable of providing a low-resistance connection between micro-channels. By contrast, if the porosity of the spongy layer decreases, the spongy layer surrounding non-percolating micro-channels becomes the limiting region of the gas transport, and thus the inclusion of micro-channels is not totally exploited: in such a case, the arrangement of micro-channels could be changed to ensure a higher percolating ratio, for example by producing longer micro-channels spanning throughout the thickness of the anode.

The achievable porosity in the spongy layer ranges from 5% to 50% or slightly higher, depending on the polymer binder volume fraction in the suspension or the usage of pore-formers. For SOFC anodes, the porosity range of 20%–35% is often adopted for the optimal performance as higher porosity values undermine the percolation of the solid phase (i.e. 30%–40% volume fraction) [55-57], thereby decreasing the active three-phase boundary (TPB) density, which is critical to lower the activation overpotential. Although the charge-transfer reaction can be sped up by larger reactant partial pressures at the reaction sites as a consequence of an optimized mass transport, this effect is often outweighed by the loss of active TPB when the spongy layer porosity is too high. Apart from the spongy layer porosity, the percolation of the micro-channels can also be improved by changing the viscosity of the suspension and using different types of bore-fluid or adjusting the radial thickness of the anode within the range of 100–600 μm. However, it is a trade-off between gas transport resistance and the mechanical strength required to resist thermal stress and cracking. These anode fabrication factors together with the design indications based on the multi-length scale analysis reported in this study can provide strategies for the microstructural optimization of tubular SOFC anodes produced by phase inversion technique.

## 4. Conclusion

This study investigated the species-independent effective transport parameters of a novel-structured tubular SOFC with the embedment of radially grown micro-channels fabricated by a phase inversion technique. For the first time, this study extracted the effective transport parameters in an SOFC system with pore size spanning over two orders of magnitude, which is considered a
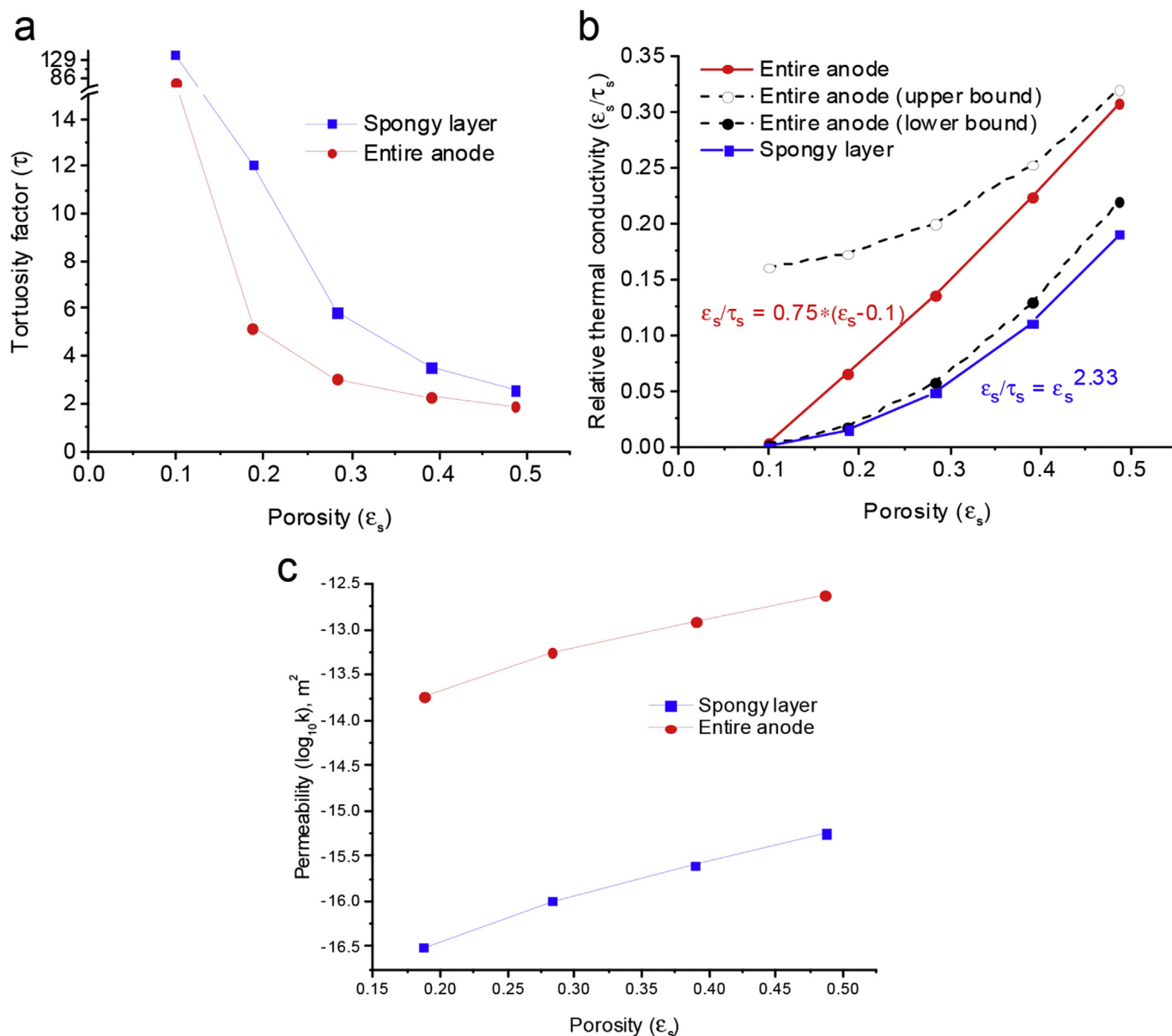
**Fig. 8.** The comparisons of the effective transport parameters between the spongy layer and the entire anode as a function of the porosity of the spongy layer.

challenge for the CFD method. This was done according to a hierarchical multi-scale approach, by imaging the microstructure at different resolutions, solving the transport equations at the nanometre length scale and then considering its effective properties in the simulation at the device level. A parametric study was also conducted to relate the tortuosity, permeability to the porosity of the spongy layer locally and globally.

The tortuous gas pathway in the spongy layer is the limiting factor of mass transport in the anode. When the spongy-layer porosity is below 10%, there is no contiguous network of the pore phase, rendering an infinite tortuosity factor. As the porosity increases from 19% to 48%, the tortuosity factor significantly decreases from 12.3 to 2.4. The variation of effective transport parameter $\varepsilon/\tau$ with porosity $\varepsilon$ follows Archie's law $\varepsilon/\tau = \varepsilon^{2.33}$, which has been improved more than ten-fold: from 0.015 at 19% to 0.19 at 48% porosity. The permeability remarkably increases from $3.1 \times 10^{-17}$ to $5.6 \times 10^{-16}$ m$^2$.

The inclusion of micro-channels significantly benefits the mass transport in the tubular SOFC. The characteristic hierarchical design of the tubular HF-SOFC anode with embedded micro-channels allows for a reduction of the tortuosity factor by 1.5—2.5 times compared to the conventional tubular SOFC anode consisting of only a spongy layer, contributing to a doubled effective mass transport parameter. The permeability was measured to improve by 2—3 orders of magnitude with the new design. These results prove the effectiveness of the micro-channels in enhancing the mass transport and mitigating the concentration polarization.

The study also shows the capabilities of multi-scale 3D tomography as an essential tool for the characterisation of hierarchical microstructures. The approach can be easily extended also to battery electrodes and membranes. Future work will leverage these new imaging and simulation tools to guide the rational design and optimization of hierarchical electrode microstructures.

### Acknowledgements

## References

[1] A. Kromp, H. Geisler, A. Weber, E. Ivers-Tiffée, Electrochim. Acta 106 (2013) 418–424.
[2] K. Eguchi, H. Kojo, T. Takeguchi, R. Kikuchi, K. Sasaki, Solid State Ionics 152 (2002) 411–416.
[3] D.J. Brett, A.R. Kucernak, P. Aguiar, S.C. Atkins, N.P. Brandon, R. Clague, L.F. Cohen, G. Hinds, C. Kalyvas, G.J. Offer, ChemPhysChem 11 (2010) 2714–2731.
[4] W. He, W. Lv, J. Dickerson, Gas transport in Solid Oxide Fuel Cells, Springer, 2014.
[5] S. Cooper, D. Eastwood, J. Gelb, G. Damblanc, D. Brett, R. Bradley, P. Withers, P. Lee, A. Marquis, N. Brandon, J. Power Sources 247 (2014) 1033–1039.
[6] B. Tjaden, J. Lane, P.J. Withers, R.S. Bradley, D.J. Brett, P.R. Shearing, Solid State Ionics 288 (2016) 315–321.
[7] J.-H. Lee, J.-W. Heo, D.-S. Lee, J. Kim, G.-H. Kim, H.-W. Lee, H. Song, J.-H. Moon, Solid State Ionics 158 (2003) 225–232.
[8] T.C. Zhang, P.L. Bishop, Water Res. 28 (1994) 2279–2287.
[9] N. Epstein, Chem. Eng. Sci. 44 (1989) 777–779.
[10] Y.-c.K. Chen-Wiegart, R. DeMike, C. Erdonmez, K. Thornton, S.A. Barnett, J. Wang, J. Power Sources 249 (2014) 349–356.
[11] Y.-c. Karen Chen-Wiegart, J.S. Cronin, Q. Yuan, K.J. Yakal-Kremski, S.A. Barnett, J. Wang, J. Power Sources 218 (2012) 348–351.
[12] S.J. Cooper, M. Kishimoto, F. Tariq, R.S. Bradley, A.J. Marquis, N.P. Brandon, J.A. Kilner, P.R. Shearing, ECS Trans. 57 (2013) 2671–2678.
[13] M. Marr, O. Kesler, J. Therm. Spray Technol. 21 (2012) 1334–1346.
[14] A. Bertei, C. Nicolella, J. Power Sources 279 (2015) 133–137.
[15] A. Bertei, C. Nicolella, ECS Trans. 68 (2015) 2887–2895.
[16] M. Ni, D.Y.C. Leung, M.K.H. Leung, J. Power Sources 183 (2008) 668–673.
[17] U. Doraswami, in, Imperial College London, 2010.
[18] T. Li, Z. Wu, K. Li, J. Power Sources 251 (2014) 145–151.
[19] T. Li, Z. Wu, K. Li, J. Membr. Sci. 449 (2014) 1–8.
[20] S.J. Cooper, T. Li, R.S. Bradley, K. Li, N.P. Brandon, J.A. Kilner, ECS Trans. 68 (2015) 1857–1864.
[21] S.M. Jamil, M.H.D. Othman, M.A. Rahman, J. Jaafar, A.F. Ismail, K. Li, J. Eur. Ceram. Soc. 35 (2015) 1–22.
[22] K. Li, Ceramic Membranes for Separation and Reaction, John Wiley & Sons Ltd, Chichester, UK, 2007.
[23] T. Li, Z. Wu, K. Li, J. Power Sources 273 (2015) 999–1005.
[24] H. Strathmann, K. Kock, Desalination 21 (1977) 241–255.
[25] S. Liu, Ceram. Int. 29 (2003) 875–881.
[26] X. Lu, B. Tjaden, A. Bertei, T. Li, K. Li, D. Brett, P. Shearing, J. Electrochem. Soc. 164 (2017) F188–F195.
[27] R. Schurch, S.M. Rowland, R.S. Bradley, P.J. Withers, IEEE Trans. Dielectr. Electr. Insulation 22 (2015) 709–719.
[28] Y. S, A.K. H, W. P, A.C. S, R.G. P, Q. W, Am. J. Roentgenol. 195 (2010) 713–719.
[29] H. Scherl, M. Koerner, H. Hofmann, W. Eckert, M. Kowarschik, J. Hornegger (Eds.), Medical Imaging, International Society for Optics and Photonics, 2007, 651058–651058-651010.
[30] J. Schindelin, I. Arganda-Carreras, E. Frise, V. Kaynig, M. Longair, T. Pietzsch, S. Preibisch, C. Rueden, S. Saalfeld, B. Schmid, Nat. Methods 9 (2012) 676–682.
[31] T.U. Kaempfer, M. Schneebeli, S. Sokratov, Geophys. Res. Lett. 32 (2005).
[32] S. Campanari, P. Iora, J. Power Sources 132 (2004) 113–126.
[33] H. Darcy, Les fontaines publiques de la ville de Dijon: exposition et application, Victor Dalmont, 1856.
[34] M. Van Droogenbroeck, H. Talbot, Pattern Recognit. Lett. 17 (1996) 1451–1460.
[35] T.M.M. Heenan, J.J. Bailey, X. Lu, J.B. Robinson, F. Iacoviello, D.P. Finegan, D.J.L. Brett, P.R. Shearing, Fuel Cells 17 (2016) 75–82.
[36] A. Bertei, B. Nucci, C. Nicolella, Chem. Eng. Sci. 101 (2013) 175–190.
[37] J.M. Zalc, S.C. Reyes, E. Iglesia, Chem. Eng. Sci. 59 (2004) 2947–2960.
[38] L. Holzer, D. Wiedenmann, B. Münch, L. Keller, M. Prestat, P. Gasser, I. Robertson, B. Grobéty, J. Mater. Sci. 48 (2013) 2934–2952.
[39] Y. Fu, in, Massachusetts Institute of Technology, 2014.
[40] B. Kenney, M. Valdmanis, C. Baker, J.G. Pharoah, K. Karan, J. Power Sources 189 (2009) 1051–1059.
[41] K.J. Yoon, S. Gopalan, U.B. Pal, J. Electrochem. Soc. 156 (2009) B311–B317.
[42] H. Zhu, R.J. Kee, J. Electrochem. Soc. 153 (2006) A1765–A1772.
[43] Y. Fu, Y. Jiang, S. Poizeau, A. Dutta, A. Mohanram, J.D. Pietras, M.Z. Bazant, J. Electrochem. Soc. 162 (2015) F613–F621.
[44] L.R. Van Loon, J. Mibus, Appl. Geochem. 59 (2015) 85–94.
[45] A. Berson, H.-W. Choi, J.G. Pharoah, Phys. Rev. E 83 (2011) 026310.
[46] J.G. Pharoah, K. Karan, W. Sun, J. Power Sources 161 (2006) 214–224.
[47] B. Tjaden, S.J. Cooper, D.J.L. Brett, D. Kramer, P.R. Shearing, Curr. Opin. Chem. Eng. 12 (2016) 44–51.
[48] J.W. Veldsink, R.M.J. van Damme, G.F. Versteeg, W.P.M. van Swaaij, Chem. Eng. J. Biochem. Eng. J. 57 (1995) 115–125.
[49] K. Yazdchi, S. Srivastava, S. Luding, in, Eccomas, 2011.
[50] A. Costa, Geophys. Res. Lett. 33 (2006).
[51] R.P. Chapuis, M. Aubertin, Can. Geotech. J. 40 (2003) 616–628.
[52] D. Osinkin, D. Bronin, S. Beresnev, N. Bogdanovich, V. Zhuravlev, G. Vdovin, T. Demyanenko, J. Solid State Electrochem. 18 (2014) 149–156.
[53] W. Pabst, E. Gregorová, in: Journal of Physics: Conference Series, IOP Publishing, 2012, pp. 012021.
[54] O.H. Wiener, Die theorie des mischkörpers für das feld der stationären strömung. 1. abhandlung: Die mittelwertsätze für kraft, polarisation und energie, BG Teubner, 1912.
[55] D. Bouvard, F. Lange, Acta Metallu. Mater. 39 (1991) 3083–3090.
[56] M. Pihlatie, Stability of Ni-YSZ Composites for Solid Oxide Fuel Cells during Reduction and Re-oxidation, VTT, 2010.
[57] N.Q. Minh, J. Am. Ceram. Soc. 76 (1993) 563–588.